Peer reviewed version

License (if available):
CC BY-NC-ND

Link to published version (if available):
[10.1016/j.compositesa.2018.09.005](#)

Link to publication record in Explore Bristol Research
PDF-document

University of Bristol - Explore Bristol Research
General rights

Finite Element Modelling of Dyneema® Composites: From Quasi-Static Rates to Ballistic Impact

Authors: Mark K. Hazzard[1, 2*], Richard S. Trask[1], Ulrich Heisserer[2], Mirre Van Der Kamp[2], Stephen R. Hallett[1]

[1]Advanced Composites Centre for Innovation and Science, University of Bristol, Queen's Building, Bristol, BS8 1TR, UK
[2]DSM Dyneema, P.O. Box 1163, 6160 BD Geleen, The Netherlands

[*]Corresponding Author: Mark K. Hazzard (mark.hazzard@dsm.com)

Abstract

A finite element methodology to predict the behaviour of Dyneema® HB26 fibre composites at quasi-static rates of deformation, under low velocity drop weight impact, and high velocity ballistic impact has been developed. A homogenised sub-laminate approach separated by cohesive tied contacts was employed. The modelling approach uses readily available material models within LS-DYNA, and is validated against experimental observations in literature. Plane-strain beam models provide accurate mechanisms of deformation, largely controlled through Mode II cohesive interface properties and kink band formation. Low velocity drop weight impact models of HB26 give force-deflection within 10% of new experimental observations, with in-plane shear strain contour plots from models directly compared with experimental Digital Image Correlation (DIC). Ballistic impact models utilising rate effects and damage showed similar modes of deformation and failure to that observed in literature, and provide a good approximation for ballistic limit under 600 m/s impact speed.

Keywords: Impact behaviour, Finite element analysis (FEA), Dyneema®

1   Introduction

Ultra-high molecular weight polyethylene (UHMWPE) fibre composites are increasingly being used in impact scenarios due to their extremely high specific tensile strength and stiffness [1]. Capturing the material behaviour through numerical modelling techniques over a range of loading conditions provides the prospect of being able to predict current performance for use as a design tool, and also provide insight into the complex deformation and failure mechanisms observed during highspeed impact [2, 3] that can

be difficult to fully capture analytically [4]. Several dimensional hierarchies exist within UHMWPE composites, with the scale of modelling used being dependent on a trade-off between the detail of phenomena required to be captured and the computational expense. Validation of current modelling techniques is also just starting to come to fruition as increased test data from mechanical tests [2, 5, 6] and ballistic impacts becomes available [7–10].

Liu *et al* [5, 11] performed a static analysis of short beam shear and long beam bending both experimentally and numerically. Numerically, a finite element plane strain 2D meso-scale model captured deformation mechanisms under quasi-static loading conditions to investigate the flexural response, utilising cohesive zones between uni-directional (UD) lamina to initiate delamination. Nazarian & Zok [12] modelled the shear response of a ±45° tension shear coupon using shell elements that were tied to rebar elements, representing the matrix and fibres respectively. This captured the scissoring of fibres under large in-plane shear deformation, however at large strains the response was too stiff. Chocron *et al* [13] modelled UD strips as well as laminates of Dyneema® HB80 by bundling the fibres together into larger macro-scale strips of solid elements representing the fibre and adjoining matrix material. Capturing the meso-microscale architecture through an increase in scale allowed the model to be more computationally efficient, however there were limitations in the overall response of the laminate, such as exhibiting a larger back-face deflection (BFD) following impact.

Continuum models can provide a reasonable alternative at reduced computational expense, however there has been great difficulty providing an accurate response, particularly when incorporating failure and damage, largely due to the poor load transfer at the fibre-fibre level caused by the low mechanical properties of the adjoining matrix, which provides attractive ballistic performance [14]. This inherent property contrasts with finite element theory, where perfect load transfer is assumed within each element. Grujicic *et al* [15] modelled $[0°/90°]_n$ impacts with homogenised solid elements using a custom continuum unit cell response based on micro-scale modelling of a single $[0°/90°]$ yarn cross over. The difficulty in capturing delamination and BFD following impact was observed. Iannucci *et al* [16] proposed a constitutive model for Dyneema® $[0°/90°]_n$ laminates, homogenising cross-ply UD layers to a shell model, providing similar deformation mechanisms with clear drawing-in of the laminate due to the low shear properties. In a detailed study with extensive material characterisation, Lässig *et al* [2] produced a non-linear orthotropic hydrocode model using a solid element continuum model for impacts

on Dyneema® HB26 in ANSYS Autodyn. Whilst results were in good agreement for the ballistic limit, BFD was unable to be captured due to the difficulty in capturing imperfect out-of-plane load transfer. Nguyen *et al* [3, 14] recently advanced this model to better capture the ballistic limit and BFD by using a sub-laminate approach, with sub-laminates separated by tied contacts in order to represent delamination. A similar sub-laminate approach has been used here, also in conjunction with an adjoining fracture mechanics based contact to represent inter-laminar matrix adhesion in LS-DYNA. For the first time, this work validates a numerical model for HB26 over a range of loading conditions, initially at low rates comparing beam stiffness to that observed in literature, followed by drop weight impact tests, and finally, ballistic impact.

2   Finite Element Modelling Philosophy

2.1   Material

The material selected, due to the large amount of data available was Dyneema® HB26, a cross-ply uni-directional laminate with approximately 80% fibre volume fraction connected by a polyurethane matrix. SK76 fibres are used with a strength of 3.6 GPa and a modulus of up to 130 GPa at $\dot{\varepsilon} > 1$. Plies of material, which are provided in a [0°/90°/0°/90°] configuration, are stacked to continue the cross-ply configuration to the required areal density and hot-pressed to adhere plies to one another and produce a hard ballistic panel. Filament diameter is unchanged by the pressing process, with each uni-directional component of the cross ply approximately 67.5 μm in thickness.

2.2   Model Description

All finite element analysis (FEA) was performed in the non-linear explicit solver LS-DYNA, with all modelling utilising version mpp971 revision 7.1.2. All models were ran using 16 processors of 2.6 GHz cores, with large models requiring high memory nodes and job times variable dependent on simulation type. Modelling HB26 at the micro-scale and meso-scale models for HB26 can be computationally expensive due to the low ply thicknesses combined with the low density of Dyneema®, which can lead to relatively thick laminates for ballistic applications containing many plies. As such a cross-ply sub-

laminate homogenisation approach, separated by cohesive tied contacts to capture inter-laminar matrix behaviour, was utilised (Figure 1).
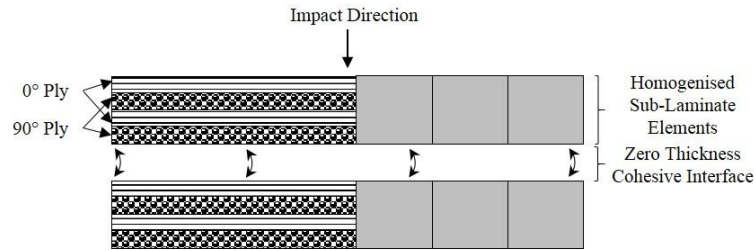

Figure 1: Schematic of the sub-laminate cross-ply homogenisation approach to capture laminate behaviour.

A hierarchical approach has been taken to investigate the model response, first selecting parameters for a homogenised response and performing single element studies (Figure 2a). Following this the laminate beam response was investigated using the sub-laminate approach, showing the dependence on the number of elements per sub-laminate and the cohesive interface properties (Figure 2b). In a separate model, experimental and model comparisons of the strain field observed in drop weight impact simulations were made, investigating the response prior to perforation of the laminate (Figure 2c). Finally, 3D ballistic impact investigations were performed, making use of the damage and failure criteria, comparing performance in terms of ballistic limit as well as BFD with literature experimental results (Figure 2d).
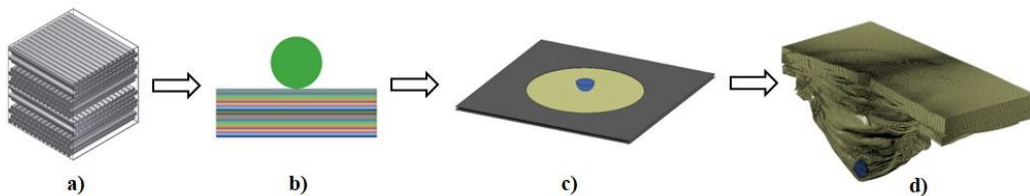

Figure 2: Hierarchical modelling approach, a) homogenisation, b) beam stiffness, c) drop weight impact, and d) ballistic impact.

2.3   Material Model

MAT162 is a commercially available composite damage and failure model produced by Materials Science Corporation [18] and accessible within LS-DYNA. It was selected to model the behaviour of the homogenised cross-ply sub-laminates. All 6 stress components contribute towards damage of the elements, based on progressive Hashin failure criteria [19] followed by strain softening, controlled by damage variables. A list of the implemented failure criteria is given in Table 1, where subscripts a, b, and

c are local element axes with a and b being in the laminate plane and c being through the thickness. Subscripts T and C denote tension and compression, and S a delamination scaling factor, and r_{7-13} are cross-ply damage thresholds [20].

Table 1: Failure Criteria in MAT162, Composite MSC [20].

Failure Mode	Criterion	
Fibre Tension/Shear (a direction)	$\left(\dfrac{\sigma_a}{S_{aT}}\right)^2 + \left(\dfrac{\tau_{ca}}{S_{aFS}}\right)^2 - r_7^2 = 0$	(1)
Fibre Tension Shear (b direction)	$\left(\dfrac{\sigma_b}{S_{bT}}\right)^2 + \left(\dfrac{\tau_{cb}}{S_{bFS}}\right)^2 - r_8^2 = 0$	(2)
Fibre Compression (a direction)	$\left(\dfrac{\sigma'_a}{S_{aC}}\right)^2 - r_9^2 = 0$	(3)
Fibre Compression (b direction)	$\left(\dfrac{\sigma'_b}{S_{bC}}\right)^2 - r_{10}^2 = 0$	(4)
Fibre Crush (c direction)	$\left(\dfrac{\sigma_c}{S_{FC}}\right)^2 - r_{11}^2 = 0$	(5)
Matrix shear (ab direction)	$\left(\dfrac{\tau_{ab}}{S_{ab}}\right)^2 - r_{12}^2 = 0$	(6)
Matrix Delamination	$S^2\left\{\left(\dfrac{\sigma_c}{S_{cT}}\right)^2 + \left(\dfrac{\tau_{bc}}{S_{bc}}\right)^2 + \left(\dfrac{\tau_{ca}}{S_{ca}}\right)^2\right\} - r_{13}^2 = 0$	(7)

Individual damage variables are coupled through the matrix q_{ij}:

$$q_{ij} = \begin{bmatrix} 1 & 0 & 1 & 0 & 1 & 0 & 0 \\ 0 & 1 & 0 & 1 & 1 & 0 & 0 \\ 0 & 0 & 0 & 0 & 1 & 0 & 1 \\ 1 & 1 & 1 & 1 & 1 & 1 & 0 \\ 0 & 1 & 0 & 1 & 1 & 0 & 1 \\ 1 & 0 & 1 & 0 & 1 & 0 & 1 \end{bmatrix} \qquad (8)$$

where i represents the 6 loading directions (damage variable) and j represents the 7 damage modes (*7-13* for cross-ply arrangement). A non-linear damage progression model is used for all damage types but is dependent on 4 pre-defined damage parameters, am_{1-4}, with subscripts being 1 for fibre damage in the a direction, 2 for fibre damage in the b direction, 3 for crush damage in the c direction, and 4 for matrix shear damage. The logarithmic damage function is given by Eq. 9:

$$E'_i = \left\{1 - \left(1 - exp^{\left(\dfrac{-r_i^{am_i}}{am_i}\right)}\right)\right\} E_i \qquad (9)$$

Where E_i is the initial stiffness, am_i is the damage factor, and r_i is the relevant damage threshold. Strain rate effects are also considered, and are captured through modification of stiffness and strength. There are 4 rate parameters, $C_{rate1-4}$, where 1 represents strain rate dependent in-plane strength, 2 represents the a

direction axial moduli, 3 represents shear moduli, and 4 represents the *b* direction axial moduli. The logarithmic law implemented is given in Eq. 10.

$$S_{RT} = S_0 \left(1 + C_{rate1} \, ln \frac{\dot{\varepsilon}}{\dot{\varepsilon}_0} \right) \tag{10}$$

where S_{RT} is the updated strength, S_0 is the original input strength, $\dot{\varepsilon}$ is the current strain rate, and $\dot{\varepsilon}_0 = 1$ is the reference strain rate. Substituting stiffness for strength in Eq. (10) provides rate dependent moduli. Element erosion can also occur, triggered by a limiting strain in directions *a* and *b*, by reaching a compressive volume limit through crushing, or through reaching a volumetric limit. Element erosion strains were selected to avoid eroding elements whilst they still contained large internal energy to limit energy loss within the system. This was done by using eroding strains that follow damage (see Figure 3 example for tension) and using high volumetric limits. The material model has previously been fully validated against ballistic testing of S2-glass composites [21], allowing for a direct comparison with HB26.

2.4   Single Element Response

The MAT162 material card information is given in Table 2 with references given for the source of the data. Further description and breakdown of how particular parameters were derived are given within this section and investigated using single element testing. As MAT162 is restricted to single integration point elements, non-physical modes of deformation can occur. To counter this an hour glassing methodology of type 6, Belytschko-Bindeman for solid elements [22], based on elastic constants with default coefficients, was used. Minimal constraints (1 node fully fixed) were placed on single elements, allowing for Poisson's contraction and expansion.

Table 2: MAT162 Dyneema® HB26 material card.

Property	Symbol	Value	Units	Ref.
Density	ρ	0.00097	g/mm^3	-
Young's Modulus aa	E_{aa}	34257	MPa	[23]
Young's Modulus bb	E_{bb}	34257	MPa	[23]
Young's Modulus cc	E_{cc}	3260	MPa	[2]
Poisson's Ratio ba	v_{ba}	0	-	-
Poisson's Ratio ca	v_{ca}	0.013	-	[2]
Poisson's Ratio cb	v_{cb}	0.013	-	[2]
Shear Modulus ab	G_{ab}	173.8	MPa	[24]
Shear Modulus ca	G_{ca}	547.8	MPa	[13]
Shear modulus cb	G_{cb}	547.8	MPa	[13]
Longitudinal Tensile Strength a	S_{aT}	1250	MPa	[25]
Longitudinal Compressive Strength a	S_{aC}	1250	MPa	-
Transverse Tensile Strength b	S_{bT}	1250	MPa	[25]
Transverse Compressive Strength b	S_{bC}	1250	MPa	-
Through Thickness Tensile Strength c	S_{cT}	1E20	MPa	-
Crush Strength c	S_{FC}	1250	MPa	[26]
Fibre Mode Shear Strength	S_{FS}	625	MPa	-
Matrix Mode Shear Strength ab	S_{ab}	1.8	MPa	[24]
Matrix Mode Shear Strength bc	S_{bc}	1.8	MPa	[24]
Matrix Mode Shear Strength ca	S_{ca}	1.8	MPa	[24]
Residual Compressive Strength Factor	S_{FFC}	0.1	-	-
Failure Model (2 = fabric cross-ply)	A_{MODEL}	2	-	-
Coulomb Friction Angle	Phi_C	0	degrees	-
Delamination Scale Factor	S_{DELM}	1	-	-
Limiting Damage Factor	OMG_{MX}	0.999	-	-
Eroding Axial Strain	E_LIMT	0.06	-	-
Eroding Compressive Volume Strain	ECRSH	0.05	-	-
Eroding Volumetric Strain	EEXPN	4	-	[27]
Coefficient of Strain Rate Fibre Strength Properties	C_{rate1}	0.0287	-	[23]
Coefficient of Strain Rate for Axial Moduli	C_{rate2}	0.1163	-	[23]
Coefficient of Strain Rate for Shear Moduli	C_{rate3}	0.225	-	[23]
Coefficient of Strain Rate for Transverse Moduli	C_{rate4}	0.1163	-	[23]
Coefficient of Softening for Axial Fibre Damage	$am1$	20	-	-
Coefficient of Softening for Transverse Fibre Damage	$am2$	20	-	-
Coefficient of Softening for Crush Damage	$am3$	20	-	-
Coefficient of Softening for Matrix Failure	$am4$	-0.8	-	[3]

2.4.1   In-Plane Tension & Compression

In-plane UD properties were approximated from quasi-static fibre and matrix properties due to the

difficulty in measuring laminate properties from non-uniform loading during mechanical tests [24]. The

rule of mixtures assuming an 83% fibre volume fraction [23] was used to determine the UD response

(Table 3), where E_{11} and E_{22} principal stiffnesses for a UD lamina, and v_{12} the Poisson's ratio, and v and E

with subscripts f and m represent fibre and matrix volume fraction and stiffness respectively. This was

then transformed to a laminate response using classical laminate analysis (CLA) which provided an equivalent homogenised [0°/90°]$_n$ response.

Table 3: Homogenising in-plane properties of HB26 under quasi-static conditions.

Property	Value	Ref.
E_f (GPa)	82	[23]
E_m (MPa)	60	[12]
v_f (-)	0.83	[24]
E_{11} (GPa)	68	-
E_{22} (MPa)	410	-
G_{12} (MPa)	86.9	[24]
v_{12} (-)	0.2832	[28]
*E_a (GPa)	34.257	-
*E_b (GPa)	34.257	-
*G_{ab} (MPa)	173.8	[24]
*v_{ab} (-)	0	-

* = cross-ply

In-plane tensile strength was approximated from single ply tests and digital image correlation of laminate tensile tests [24, 25]. The in-plane damage parameter ($am_1 = am_2 = 20$) was selected to minimise energy absorption post damage, similar to that observed in single fibre, yarn, and ply tests [23, 25], represented in Figure 3.
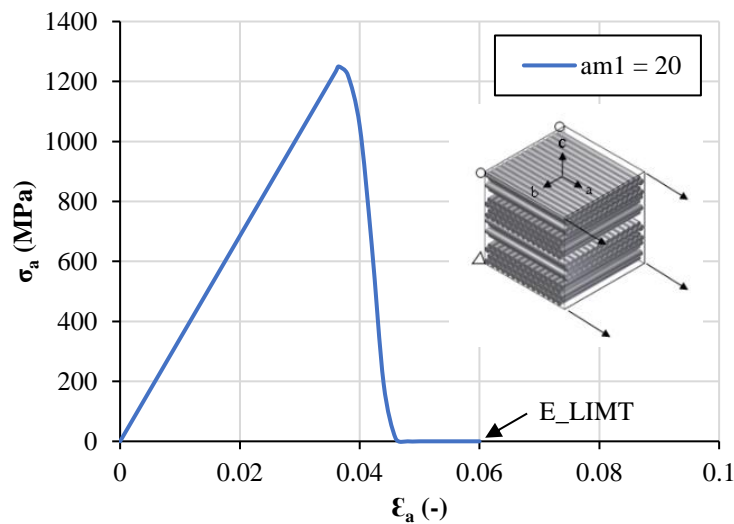
Figure 3: The effect of the in-plane damage parameter for MAT162 with HB26 properties.

In-plane compression of laminates has been shown to initiate micro-buckling and kink-band formation occurring at a low stress compared with tension [29]. The compressive in-plane strength was assumed

8

equal to that in tension, and the kink band formation and buckling was captured at the laminate level through deformation of individual sub-laminates.

The effects of strain rate were estimated from yarn tests by Russell *et al* [23]. As the reference strain rate cannot be altered from unity, the unit time of the simulation must be set to a suitable unit (milliseconds). $C_{rate1-4}$ were determined from a logarithmic fit of non-dimensionalised experimental results which highlight the effect of the C_{rate1} on in-plane tensile strength (Figure 4). In-plane axial moduli are controlled through C_{rate2} and C_{rate4} in the longitudinal and transverse direction respectively (Figure 5).
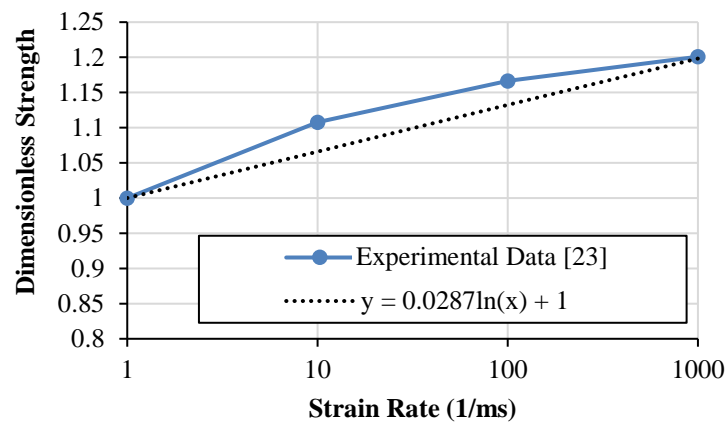
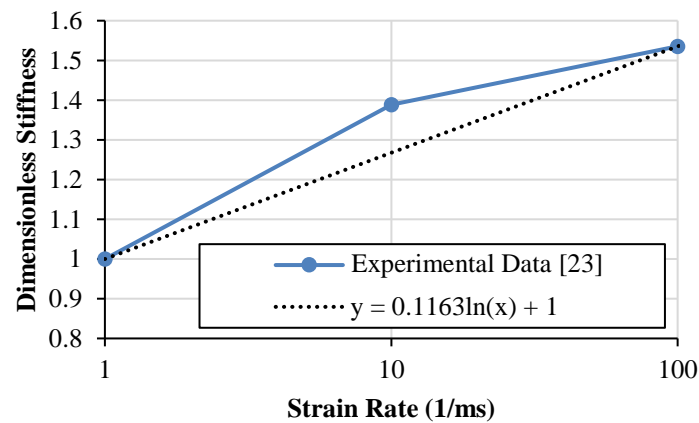*Figure 4: Longitudinal strength determination of strain rate parameter C_{rate1}.*

Figure 5: The effect of C_{rate2} and C_{rate4} on the tensile longitudinal and transverse moduli.

2.4.2   In-Plane Shear

The in-plane shear behaviour during ±45° tensile testing was dominated by fibre re-orientation [24], which for a homogenised [0°/90°]$_n$ cross ply must be included in its response. An initial modulus based

on experimental results followed by matrix shear damage was implemented [24]. At large strains, non-linearities caused by fibre re-alignment and scissoring become important [24], requiring invariant node numbering which allows the local elemental axis to rotate. However, this does not capture scissoring leading to an angle reduction between principal axes (Figure 6).
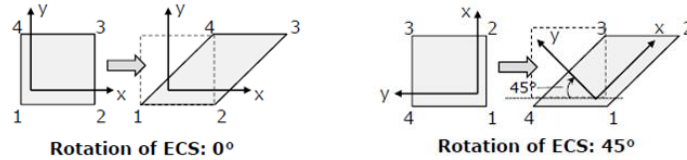

Figure 6: Example of the element coordinate system(ECS) with no invariant node numbering and with invariant node numbering [30]*.*

As such, fibre scissoring must be included within the material model itself to account for additional energy absorption. A negative damage parameter in equation 9 has been utilised allowing elements to absorb strain energy following in-plane shear damage. Shear testing of ±45° specimens highlighted a large dependency of strength on the gauge region geometry [3, 17, 24] . As this model is to be used in impact scenarios with large laminate widths (complete in-plane shear failure not observed), the data for the largest available gauge width was utilised [3]. MAT162 negative damage parameters allow stiffness to be altered and approach a new asymptote, however it is limited in terms of fully capturing the non-linear shear deformation observed in testing. As such the experimental strain energy absorbed up to $\gamma_{ab} = 1.2$ [3] was approximated by using a damage parameter of *am4 = -0.8*. Comparisons to experimental observations are given in Figure 7.
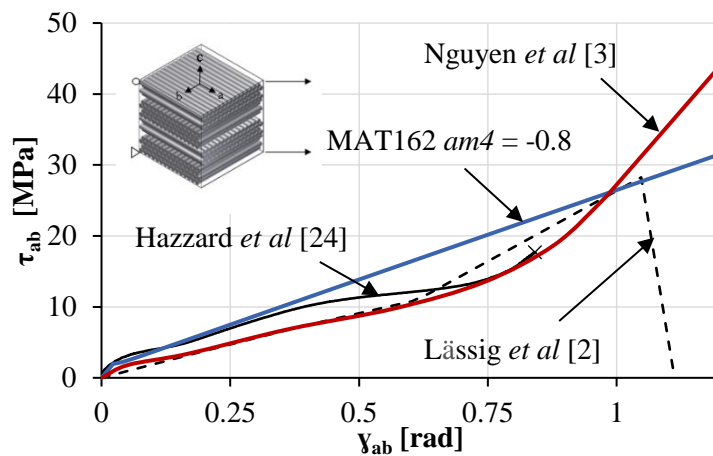

Figure 7: The effect of a negative damage parameter on the shear response of a single element.

A strain rate parameter for shear stiffness was estimated in the same manner as the in-plane response, but with only a limited data set available [24]. The rate effect was larger than in-plane tension as this is a matrix dominated property, with $C_{rate3} = 0.225$ (Figure 8).
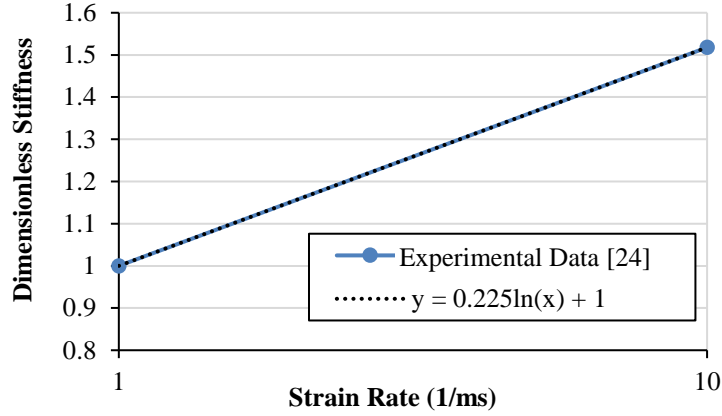

Figure 8: The effect of strain rate on shear stiffness.

2.4.3 Through Thickness Shear

The through thickness shear properties of HB26 are difficult to measure, largely due to the inability to transmit load by the low shear strength matrix [2]. This mode of laminate deformation is a micro-response that may not be able to be captured in a single homogenised element. Here, the MAT162 stiffness has been approximated, based upon fibre volume fraction, assuming negligible contribution of the matrix and transverse fibres (Table 4). Transverse fibre stiffness (G_{32f} of 90° fibres loaded in shear) was assumed to have negligible contribution in G_{ca} for [0°/90°]$_n$ homogenised laminates due to the difficulty in loading fibres in this manner. As the element is a homogenised cross ply, $G_{ca} = G_{cb}$.

Table 4: Homogenised through-thickness properties derived from fibre shear properties.

Property	Value	Ref.
G_{31f} (MPa)	1320	[13]
v_f (-)	0.83	[24]
G_{31} (MPa)	1095.6	-
G_{ca} (MPa)	547.8	-
G_{cb} (MPa)	547.8	-

The through thickness matrix shear strength has been set equal to the in-plane matrix shear strength, as this is a matrix dominated property. Therefore $S_{ca} = S_{cb} = S_{ab} = 1.8$ MPa [14, 24], with the response given in Figure 9. A coulomb friction angle can be implemented in MAT162, however $\varphi = 0$ was selected due

to the low coefficient of friction of Dyneema® HB26. Delamination scale factor S which is used to control delamination zone size has been left as default value of 1. A negative shear damage parameter am_4 = -0.8 was also used for calculating shear stress in the through thickness direction after damage. Through thickness shear stress also contributes to in-plane fibre failure through the quadratic interaction of stresses. Maximum shear stress was approximated through principal stress theory based on in-plane tension, which was equal to half of in-plane tensile strength, i.e. 625 MPa.
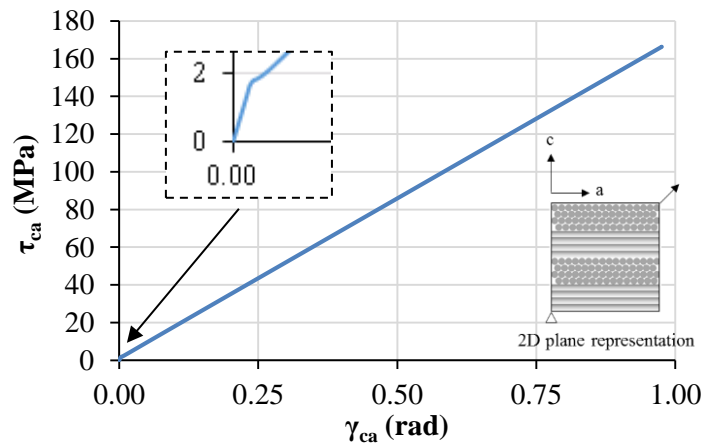

Figure 9: Through thickness shear response

2.4.4 Through Thickness Compression and Tensile Response

Through thickness stiffness was approximated from plate flyer impact tests by Lässig *et al* [2], with E_c = 3620 MPa. Assuming an indirect tension mechanism drives failure [26], through-thickness compressive strength was estimated to be equal to cross-ply tensile strength σ_c = 1250 MPa. The crush damage parameter, am_3 = 20, was selected to provide an identical failure response to that of in-plane tension; once fibres have failed little energy absorbing capability remains, with the single element response shown in Figure 10.
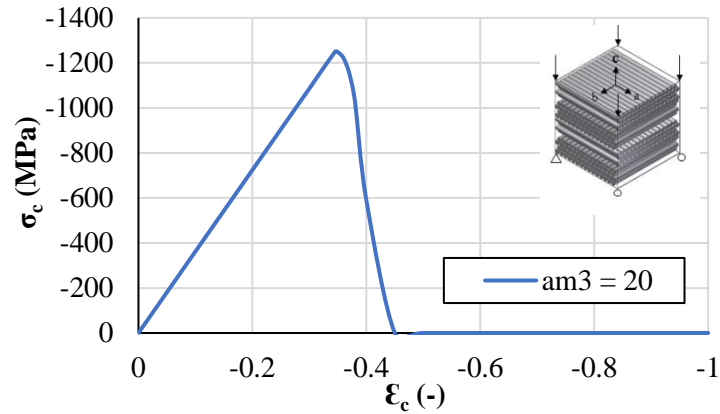
Figure 10: The effect of crush damage parameter.

2.5   Cohesive Interface Model

Sub-laminates were joined together through cohesive tied contacts using automatic surface to surface tiebreak contact with option 9 to represent limited load transfer capability. The sub-laminate cohesive model utilises a mixed mode rate independent fracture mechanics approach with Mode I and Mode II interaction with a bi-linear traction separation law [30]. Due to the low bending stiffness of Dyneema®, a custom experimental methodology is required to accurately capture cohesive properties [31]. Cohesive interface initial stiffness was approximated by assuming the cohesive interface size was equal to the sub-laminate height (distance between cohesive interfaces). This was equivalent to assuming poor matrix load transfer throughout the sub-laminate (Eq. 11).

$$K_I = \frac{E_m}{t_{SL}} \qquad (11)$$

Where K_I is Mode I traction stiffness, E_m is the Young's modulus of the matrix material, and t_{SL} is the thickness of the sub-laminate. K_{II} was approximated through using a stiffness ratio of $K_I/K_{II} = 0.6$ which provided an adequate stiffness response during short beam shear investigations based on K_I input. A graphical response is given in Figure 11 and the full cohesive interface contact card given in Table 5.
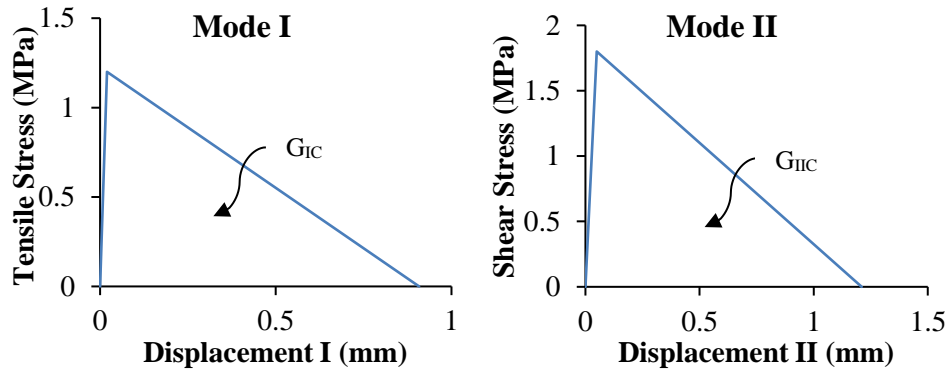
13

Figure 11: Cohesive interface model for Mode I and Mode II cohesive contact with a sub-laminate thickness of 1 mm, at quasi-static rates.

Table 5: Quasi-static tied contact cohesive interface model input card, 1 mm sub-laminate thickness.

Property	Symbol	Value	Ref.
Mode I Tensile Strength** (MPa)	T	1.2	[2]
Mode I Initial Stiffness* (N/mm^3)	K_I	60	-
Mode I Fracture Energy (N/mm)	G_{Ic}	0.544	[32]
Mode I Traction Max' Displacement (mm)	D_{IF}	0.908	-
Initial Stiffness Ratio (-)	K_{II}/K_I	0.6	-
Mode II Shear Strength** (MPa)	S	1.8	[14, 24]
Mode II Fracture Energy (N/mm)	G_{IIc}	1.088	
Mode II Traction Max' Displacement (mm)	D_{IIF}	1.21	-
Exponent of Powerlaw (-)	PARAM	1	[30]

* Initial stiffness dependency upon element size
** Quasi-static strength

3   Beam Deformation Investigations

Cantilever loaded beams were modelled to investigate the effective bending stiffness of HB26 as a means of validating the deflection following impact. The modelling approach was also investigated by varying the number of elements per sub-laminate as well as the thickness of each sub-laminate. Two experiments performed by Liu *et al* [5] were used for comparison, with the experimental setup given in Figure 12. The width of all beams was 20 mm, the loading cylinder diameter *d* was 6.4 mm at a distance *s* of 10 mm from the free end and the total laminate height *h* was 6 mm. Loading was performed with a constant displacement rate of 2mm/min, for beam lengths *L* of 10 mm and 100 mm, giving a short beam shear test and a long beam bending test respectively. All modelling used one solid element with a single integration point across the width, with plane strain boundary conditions. For beam studies, rate effects were set to zero and the displacement rate was increased to 0.05 mm/ms to reduce computational expense. All beams

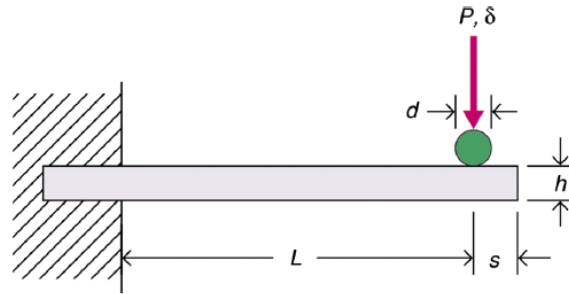were fully clamped at one end during the experiment, represented here by fully fixed boundary conditions.

Figure 12: Experimental setup for beam studies performed by Liu et al [5].

3.1   Short Beam Shear

Short beam shear models with a relatively low L/h and an initial sub-laminate thickness, t_{SL}, of 0.25 mm (Figure 13) were investigated first.
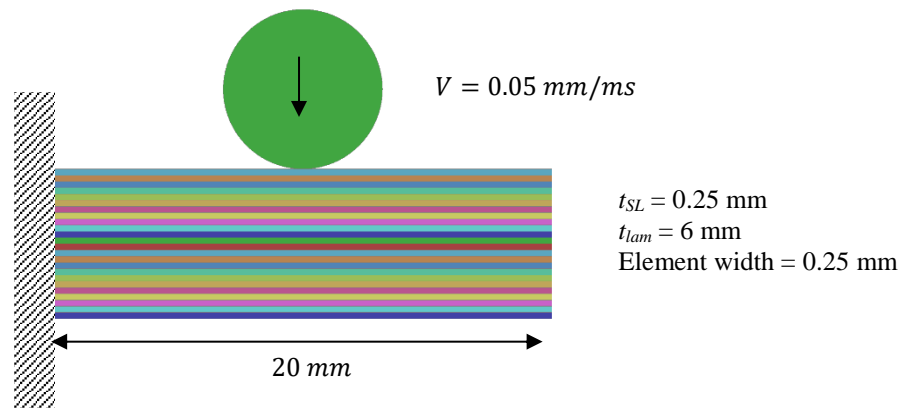

Figure 13: Representative short beam shear model from experimental tests [5].

The number of elements through the thickness of each sub-laminate was varied as 1, 2 and 3 elements (Figure 14). Initial stiffness was identical to that observed experimentally, however, after reaching the maximum Mode II cohesive interface strength multiple elements per layer were too stiff. This was due to the build-up of bending stress, in contrast a single element layer effectively provides a direct bending stress of zero due to its single integration point. Normally multiple elements through each sub-laminate thickness would be required, however the inability of Dyneema® fibres to take compressive loads and instead micro-buckle limits the capability for bending stress to build up in the microstructure. Therefore, the inability of single element layers to capture bending stress distribution provides a reasonable

approximation to the short beam post-cohesive shear damage response. Under loading this promoted buckling of sub-laminates and limited shear stress transfer within the sub-laminate (Figure 15), comparable to that observed during experimental observations [5]. One element thick sub-laminates were therefore used for all modelling techniques following this investigation.
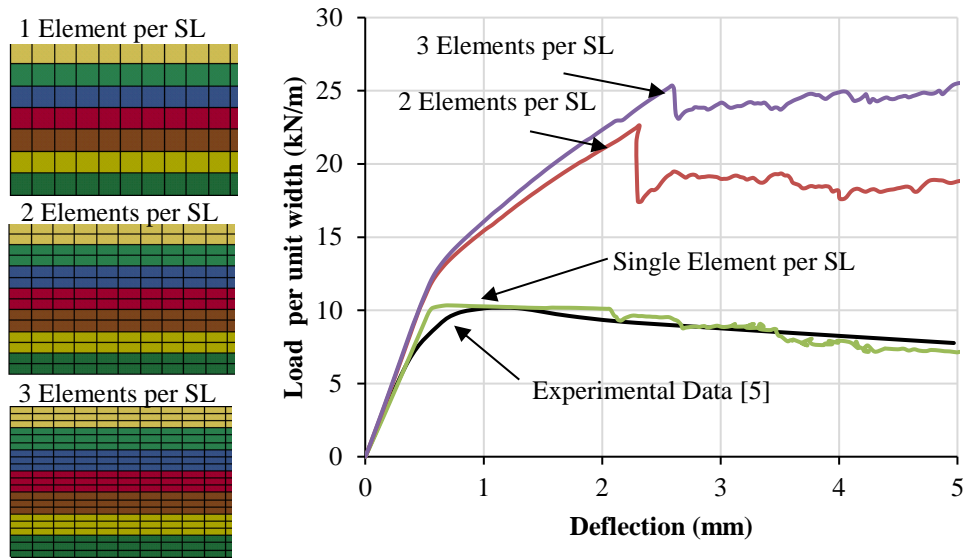

Figure 14: Effect of short beam shear response on the number of elements per sub-laminate (SL).
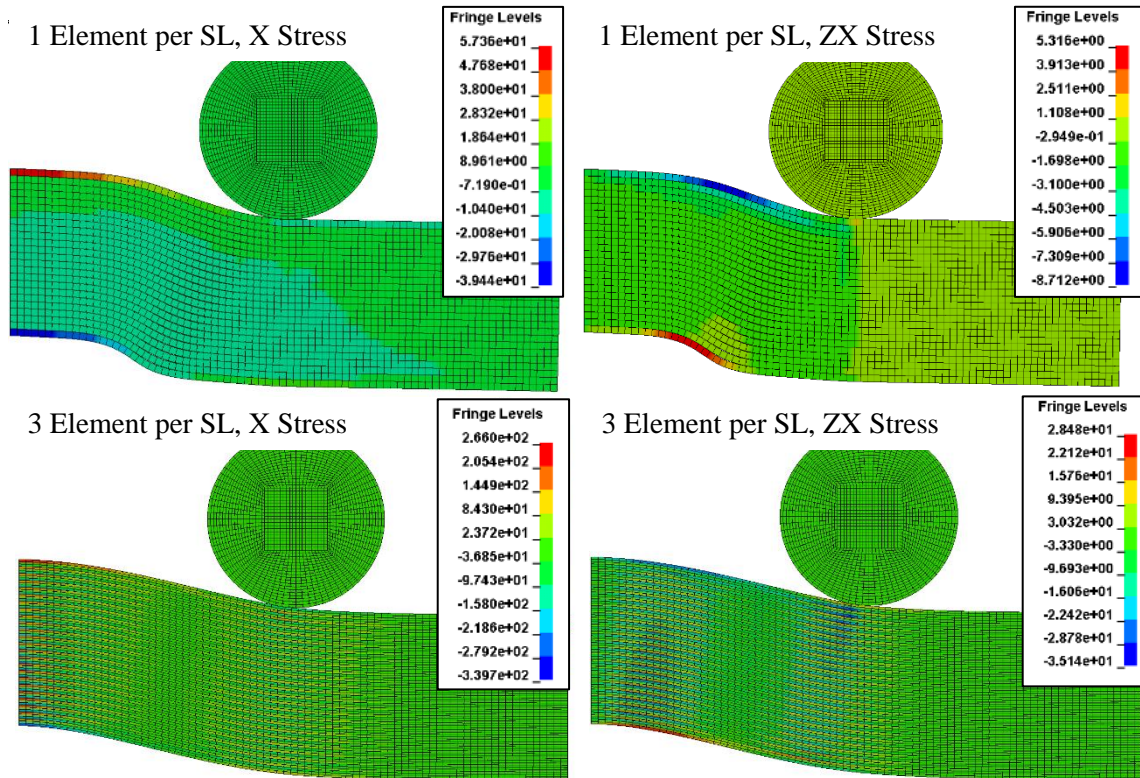
Figure 15: Comparison of axial stress (MPa) and through thickness shear stress (MPa) build up in sub-laminates for 1 element per sub-laminate (SL) and 3 elements per sub-laminate at 2 mm deflection.

The inability to carry further transverse load was triggered by damage to the cohesive interface, controlled by the Mode II inter-laminar response. Prior to reaching Mode II shear strength of the cohesive interface (Figure 16a) the response was controlled by a combination of the shear stiffness of the cohesive interface and the shear stiffness in the sub-laminate. Nodes connected by the cohesive interface develop displacements relative to one another in the elastic region of the cohesive contact rather than pure shear of elements themselves (Figure 16b). The lack of load transfer between sub-laminates was representative of the lack of load transfer between fibres, with fibres having a higher shear stiffness compared with the matrix. After reaching maximum Mode II cohesive strength, gradual failure of the cohesive interface can ensue, with total failure of some cohesive interfaces occurring just past 2 mm vertical displacement, allowing sub-laminates to separate (Figure 16c). The initialisation of reduced load bearing capability was investigated by varying mode II cohesive interface strength. Increased mode II shear strength postponed inter-laminar damage and increased the load required to delaminate the beam, with the effect on load deflection curves indicated in Figure 17.
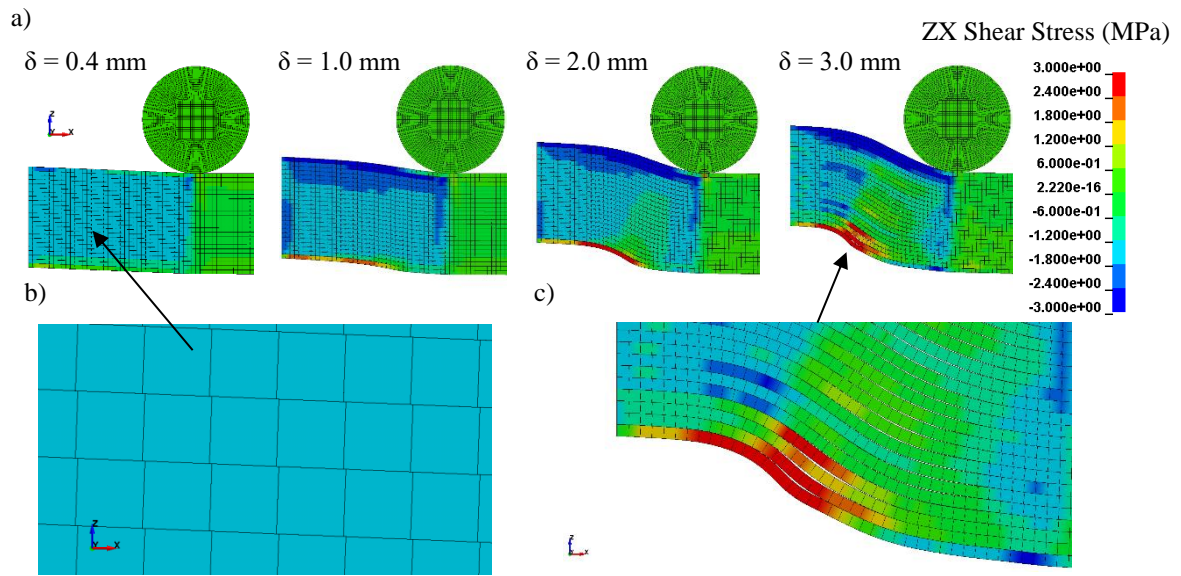
Figure 16: Finite element modelling of short beam shear deformation, a) as displacement progresses, b) cohesive elastic deformation, and c) cohesive interface failure.
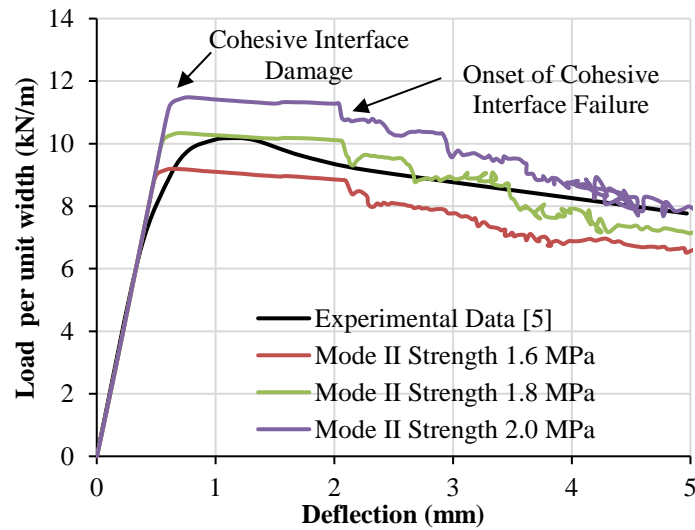

Figure 17: The effect of Mode II cohesive shear strength on short beam shear response.

Variation of sub-laminate thickness, and hence number of sub-laminates in a given beam, with different cohesive interface stiffness was investigated. This showed that with increasing sub-laminate thickness a proportional reduction in cohesive interface stiffness was required to provide the same beam initial stiffness (Figure 18). The sub-laminate thickness also influenced the post cohesive damage response, reducing load bearing capability when the sub-laminate thickness was reduced below 0.125 mm. Smaller sub-laminate thicknesses, approaching a single UD layer thickness, were beyond the scope of homogenised cross-ply investigations.
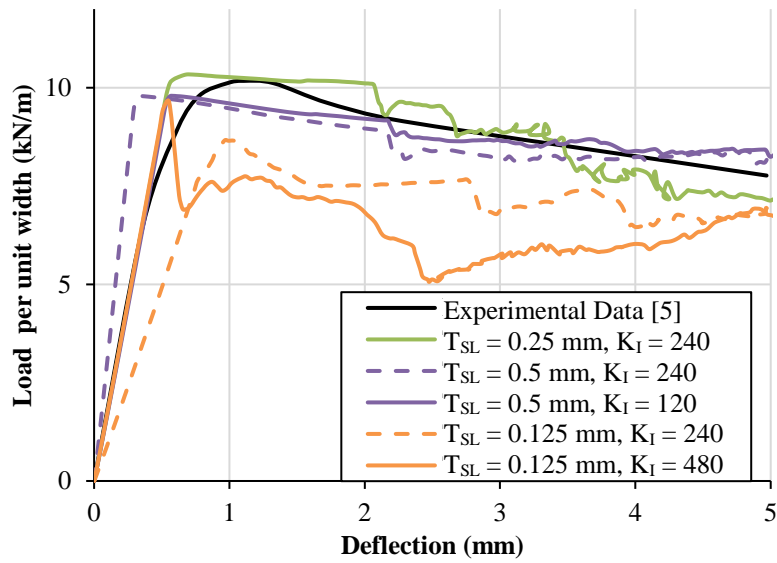
Figure 18: The effect of varying sub-laminate thickness (T_{SL}) and cohesive stiffness (K_I related to K_{II} by a factor of 0.6).

3.2   Long Beam Buckling

Longer beam bending experimental results (L = 100 mm, Figure 12) [5] were modelled with the same parameter set, maintaining a sub-laminate thickness of 0.25 mm. As in experimental observations, the load bearing capability was controlled by kink-band formation at the root of the beam (Figure 19). The size and shape of the kink-band was larger in modelling than in experimental observations, thought to be due to the inability to capture micro-scale phenomena such as micro-buckling of fibres and individual lamina deformation. This effectively led to an increase in the load required to buckle the beam at the root (Figure 20). Numerical noise post-buckle was induced due to the relatively coarse element size compared with that required to capture this micro-driven phenomenon. However, the post-buckle average load does plateau to a similar value to that from the experiments.
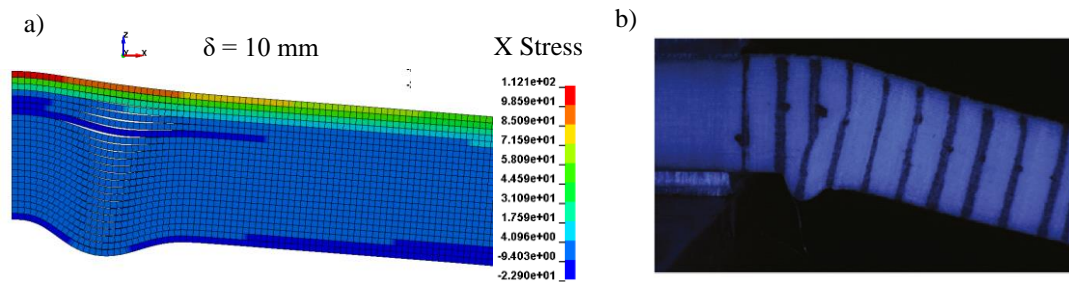

Figure 19: Root buckle of long beam bending. a) Modelling at deflection δ = 10 mm and b) experimental observations from Liu et al [5].
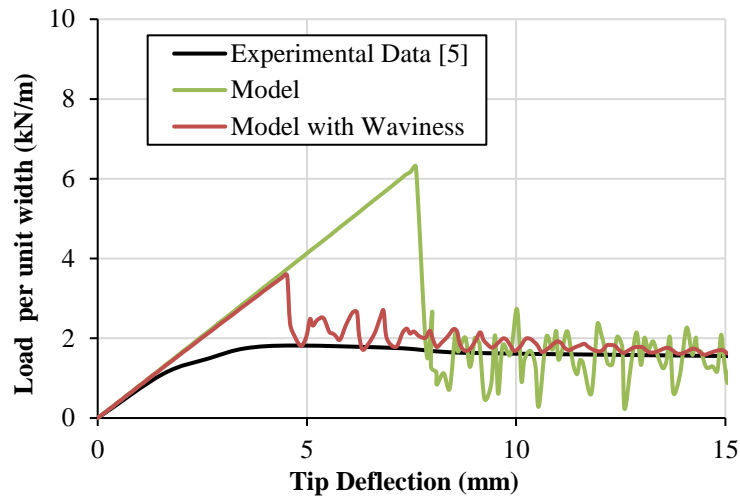
Figure 20: Longer beam bending load-displacement response, and the effect of introducing ply waviness.

One conclusion from experimental observations was that ply waviness may be a contributing factor, helping to initiate the buckling response through out of plane fibre variations observed in the microstructure. To replicate this, waviness was input into the element co-ordinate system by altering the local material axes in the element keyword card. The degree of ply waviness was approximated from microstructural investigations [24], assuming a sinusoidal wave input in the form:

$$y(x) = A \sin(\omega x) \qquad (12)$$

Where A is the amplitude of the sin wave, and ω is the frequency of oscillation, equal to 0.14 mm and 0.93 rad/mm respectively. The physical representation is similar to an optical microscope image of a HB26 laminate cross section (Figure 21). Incorporating ply waviness reduced the initial buckling load by approximately half, bringing it closer to that observed in experiments [5] and reduced oscillations in the signal (Figure 20).
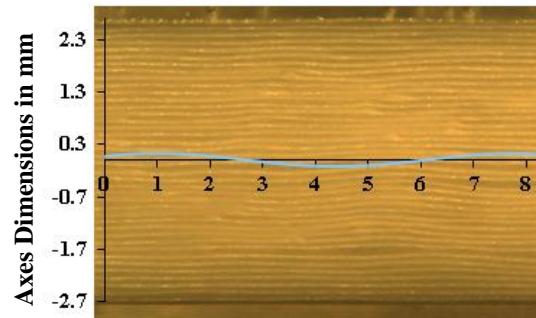
Figure 21: Sinusoidal ply waviness approximation overlaid with optical microscopy [24]*.*

Although the post buckle response was similar, the beam still buckled at a higher a load compared with experimental results. The effect of micro-buckling of the fibres was difficult to capture at the model's scale, and needs to be investigated further to accurately capture this phenomenon. It was thought that this will have little effect on the modelling of ballistic impact on UHMWPE fibre laminates for validation purposes as the projectile has come to rest prior to the transverse shear wave reaching the boundary (boundary effects have limited effect on the ballistic performance).

4 Drop Weight Impact Modelling

Drop weight impact testing, without failure of the fibres, was investigated by Hazzard *et al* [6].These results were used to compare the in-plane shear response to that predicted by the finite element model. The experiment impacted HB26 laminates 32 UD plies thick (2.2 mm thickness) with a 150 J blunt hemispherical impactor. Purely frictional clamping of the 200 mm^2 laminates around a 125 mm diameter aperture constrained the laminate, replicated in LS-DYNA by modelling the entire laminate, clamp, and blunt hemispherical impactor (Figure 22a). An initial velocity was given to the impactor of -3.377 m/s, with a density of the impactor material to simulate a mass of 26.3 kg, totalling 150 J impact energy. Clamps were modelled with a single element through the thickness (1 mm thick), with both the impactor and clamps using a rigid material, as deformation of the impactor and clamp did not occur. The lower clamp was fully constrained whilst the top clamp had an equivalent pressure load on its top surface to provide 2 MPa pressure over the laminate contact area. This was equivalent to controlling the clamping pressure experimentally through torque tightening of surrounding bolts during the experiment. Contact was applied between the clamps and the laminate with a static and dynamic coefficient of friction of 0.1

(Figure 22b). The laminate itself was discretised into sub-laminates with thickness of 0.1375 mm, equivalent to a single [0°/90°] cross-ply of Dyneema® (Figure 22c-d). Cohesive interfaces, with stiffness adjusted according to Eq.11, were inserted between each layer of sub-laminates. The in-plane laminate element dimensions were 1×1 mm and matched by that of the impactor, and an eroding surface contact was used between in the impactor and laminate in case of element failure (none expected from experiments). Identical material properties within each sub-laminate were used as in the beam test modelling, with rate effects now turned on (Table 2).
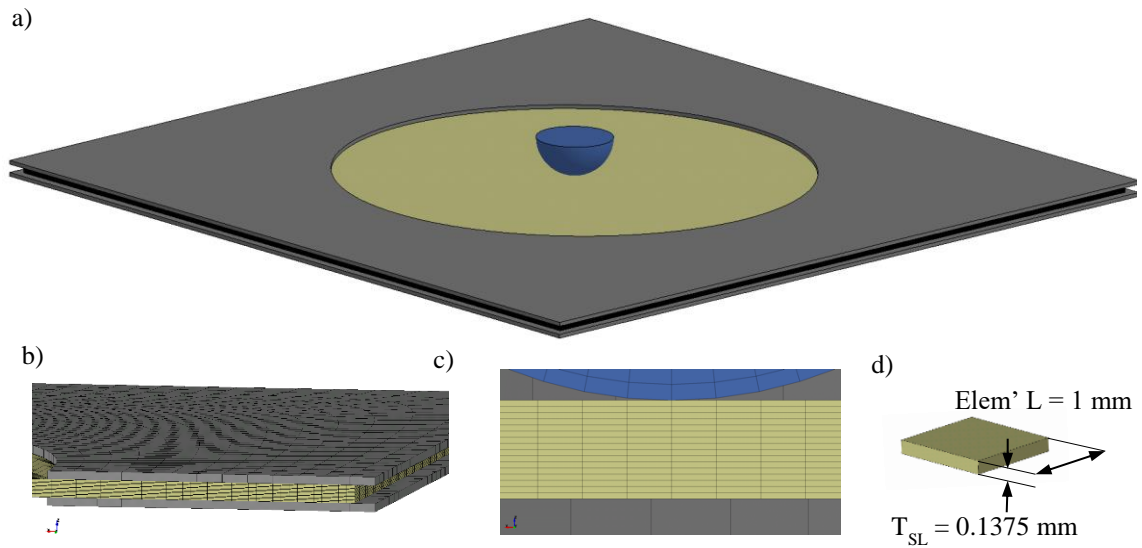

Figure 22: a) Isometric view of drop weight impact model, b) cross-section highlighting clamp conditions, c) cross section highlighting mesh density through the thickness, and c) element size utilised within the laminate.

4.1 Drop-Weight Model Results

The predicted force-deflection results from the finite element analysis were similar to experimental results (Figure 23). Maximum BFD for the [0°/90°]$_{16}$ laminate was almost identical; however the maximum contact force was approximately 10% larger in the model. Energy absorbed was also within 10%, however a larger rebound is observed within the model as gravity has not been applied. Initially the contact force was lower, thought to be caused through excess in-plane shear strain of the model compared with that of the experiment, visualised by a full field strain comparison with time in Figure 24. Although strains were of the same magnitude, locally higher in-plane shear strains were observed around the boundary and close to the point of impact. It is thought that the inability to fully capture the in-plane shear curve can lead to locally higher shear strains, whilst the relatively simple boundary model does not

capture the potential variation in coefficient of friction in static and dynamic loading with the dependence on boundary pressure. Modelling was also able to show that the largest in-plane shear deformations tended to occur under the boundary itself, something that couldn't be captured by digital image correlation during experiments. Larger scale wrinkling was also visible in the model (Figure 24), thought to be due to the relatively large in-plane element dimensions compared with the length scale of the wrinkles observed during testing. The out-of-plane curvatures in experiments with a scale of less than 1 mm in length could therefore not be captured. Instead the wrinkles form at a larger scale due to the larger elements and a higher compressive strength/stiffness within the sub-laminates. The formation of the wrinkles was thought to limit shear deformation in certain areas, effectively increasing laminate stiffness at greater deflection values and increasing contact force (Figure 23).
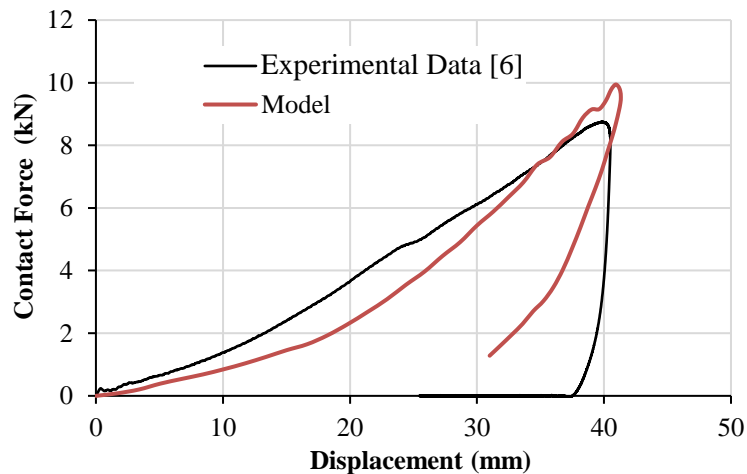

Figure 23: Force-deflection curve comparison from HB26 drop weight impact test and FEA model.
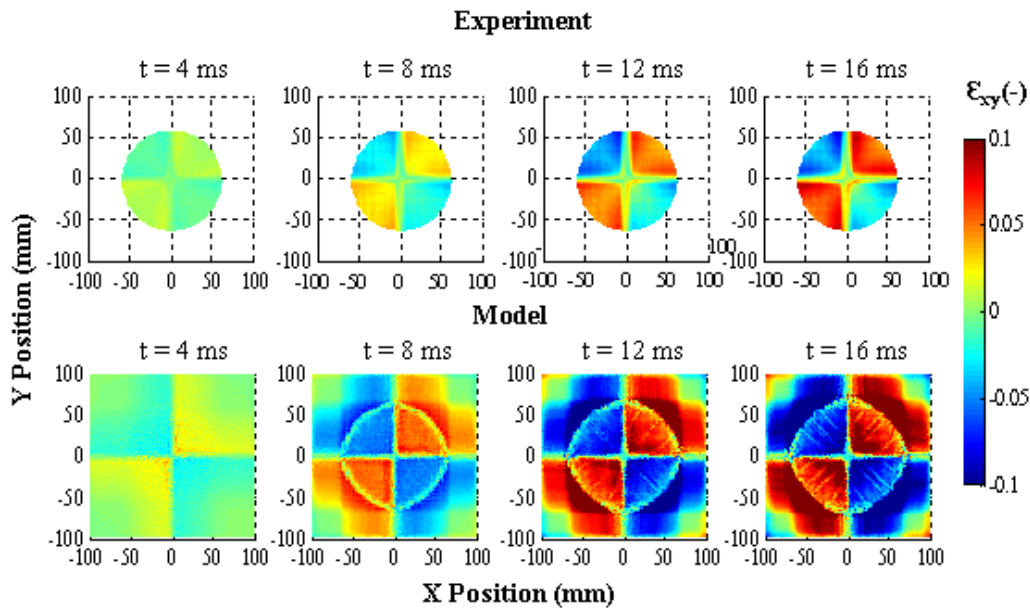
Figure 24: HB26 drop weight impact in-plane shear strain contour map comparison of experimental results recorded via DIC compared with model results with varying time after impact.

5   Ballistic Impact Modelling

Following on from low rate modelling, ballistic impact modelling of Dyneema® was compared with open

literature experimental data. Nguyen *et al* [7] impacted target laminates with in-plane dimensions of

300×300 mm with varying thickness. The projectile used was a 20 mm diameter fragment simulating

projectile (FSP) at a range of impact velocities, providing a ballistic limit approximation through a

Lambert-Jonas approximation [33]. Laminates were modelled with an identical approach as previously

described, with no boundary constraints surrounding the laminate. Although the boundary was clamped

during the experiment, the effect of the clamping condition was thought to be minimal as the plate was

large enough for the projectile to come to rest prior to the transverse shear wave reaching the boundary

combined with the low coefficient of friction of Dyneema®. A biased mesh was incorporated, increasing

mesh density towards the impact zone (central 20×20 mm), with the elements in this zone being cubic to

provide the optimum aspect ratio for failure analysis (Figure 25). In all ballistic analyses an identical

material and contact card to previous models was used, as in Table 2 and Table 5, with one exception;

shear strength in the material model as well as the cohesive interface strength was increased from 1.6 to

2.6 MPa, equivalent to that found at higher rate experiments, similar to those observed during ballistic impact [14].
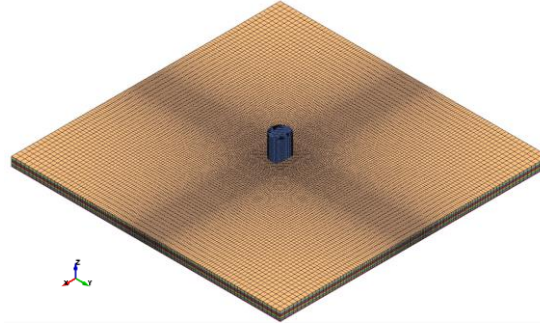

Figure 25: Projectile and target mesh.

During analyses, it was found that there was a contact issue regarding interpenetration of sub-laminates resulting in large negative contact energies, thought to be caused by a rate effect with the surface contact algorithm related to low stiffness properties of the cohesive formulation. Previous studies have found a similar issue, and modelled laminates with gaps in-between sub-laminates to prevent inter-part penetration [3]. Here an additional automatic surface to surface contact with default options and an updated contact algorithm was applied to maintain a gapless approach between sub-laminates.

5.1   Projectile Model

The FSP had a mesh size equal to that of target laminate impact zone to avoid any contact mismatch through varying mesh density. The FSP was represented using the simplified Johnson-Cook material model MAT98 in LS-DYNA, with identical parameters to that used by Nguyen *et al* [3], given in Table 6.

Table 6: MAT 98 material model for 20 mm diameter FSP [3].

Property	Symbol	Value	Units
Density	ρ	0.0078	g/mm^3
Young's modulus	E	207000	MPa
Poisson's ratio	v	0.33	-
Yield stress	A	1030	MPa
Hardening constant	B	477	MPa
Hardening exponent	N	0.18	-
Strain rate constant	C	0.012	-
Effective plastic strain at failure	$\mathcal{E}_{PF}$	1E17	MPa
Maximum stress before rate effects	σ_x	1E20	MPa
Saturation Stress	σ_{SAT}	1E20	MPa
Reference strain rate	$\dot{\varepsilon}_0$	1	s^{-1}

5.2   Mesh Refinement Study

A mesh refinement study was performed to determine the dependency of the element geometry on the ballistic performance of the laminate. Here, depth of penetration (DOP) has been investigated on 50 mm thick target laminates, followed by the ballistic limit (V_{BL}) and BFD of thinner 10 mm target laminates. Meshes produced in all studies maintained an element aspect ratio of unity in the impact zone. During beam studies, it was highlighted that single element sub-laminates more accurately represent the near zero bending stiffness of Dyneema®. This meant that increasing the mesh density also increased the number of sub-laminates within the model. The cohesive interface has therefore had its initial stiffness K_I updated in accordance with Eq.11. The biased mesh with increasing element size approaching the edge of the laminate had a maximum in-plane dimension of 5 mm and a maximum aspect ratio of 5.

Firstly, DOP studies were performed on 50 mm thick laminates at an impact speed of 500 m/s. Cubic sized central elements varying from 1 mm to 5 mm resulted in the sub-laminate thickness being the same as the in-plane element dimensions to maintain an aspect ratio of unity, see Table 7. A relatively thick laminate was chosen to investigate the progressive failure regime prior to large membrane deflection, with DOP defined as the thickness of the number of layers that failed. DOP was found to increase with increasing mesh density, partly due to large elements giving limited resolution in terms of failure of the sub-laminate thickness. Convergence of the mesh was found at approximately 1 mm in size with DOP being within 2 mm of the next largest element size (Table 7). The change in velocity of the projectile with time also highlights the mesh convergence at higher mesh densities (Figure 26). The largest mesh produced a stiffer response, decelerating the projectile at a faster rate with a lower DOP.

Table 7: DOP mesh study input parameters at 500 m/s impact velocity of a 50 mm laminate target.

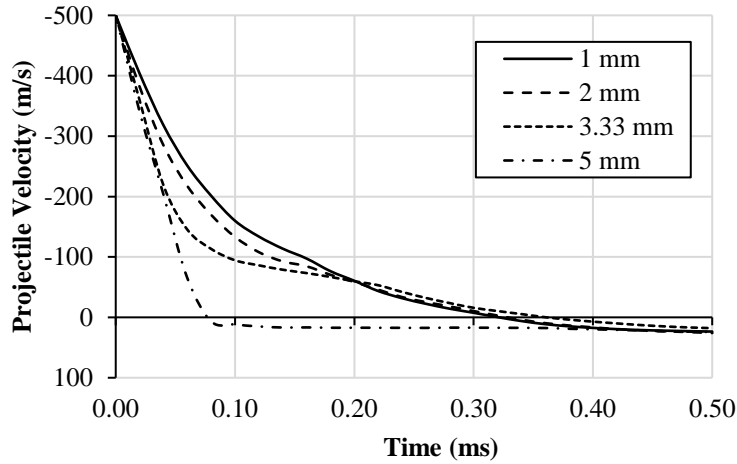| Impact Zone Element Size (mm)	No. Sub-Laminates	K_I^* (N/mm³)	Outer Element Aspect Ratio	DOP (mm)	% Diff' from next largest mesh
5	10	12	1	5	-
3.33	15	18	1.5	10	50
2	25	30	2.5	14	28.6
1	50	60	5	16	12.5

* From equation 11

Figure 26: Projectile velocity time trace for varying mesh densities during DOP investigation.

Mesh dependency of V_{BL} and BFD of thinner laminates was also investigated with the 20 mm FSP. All laminates were 10 mm thick, whilst impact velocity was varied to provide a minimum of 3 residual velocity (V_R) values following perforation to estimate V_{BL} using the Lambert-Jonas approximation in Eq.13.

$$V_R = a\left(V_I^p - V_{BL}^p\right)^{1/p} \qquad (13)$$

where V_I is the initial velocity, and a and p are selected through a least square curve fit with V_{BL} estimated at $V_R = 0$. Mesh parameters for the thinner target tests are provided in Table 8. The investigation showed that reducing mesh size lowered V_{BL}, with the smallest mesh sizes of 1 mm and 0.66 mm within ±10% of one another. This was not a full convergence, which highlights that bulge failure at the rear of the laminate was more susceptible to mesh variation than progressive failure in DOP tests. Due to the limitations in runtime, computational cost, and the physical mesh size approaching that of a UD model, smaller mesh sizes were not investigated. The Lambert-Jonas least square fit of results is also given in Figure 27, highlighting the variation induced in V_{BL} by changes in mesh geometry.

Table 8: Mesh sensitivity of V_{BL} for a 10 mm laminate target.

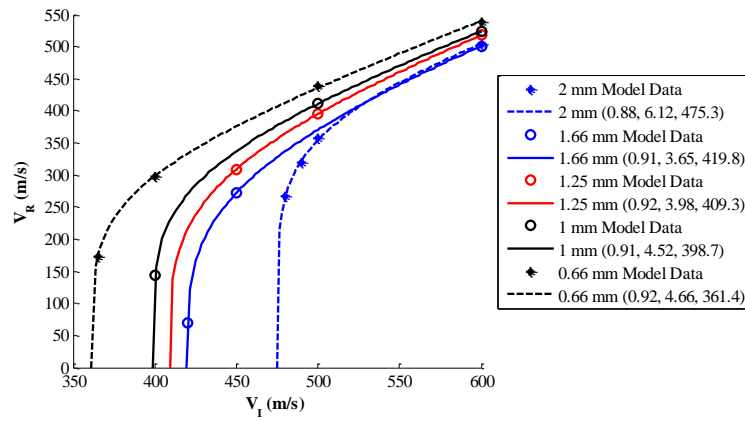| Impact Zone Element Size (mm)	No. Sub-Laminates	K_I (N/mm³)	Outer Element Aspect Ratio	Approximate V_{BL} (m/s)	% Diff' from next largest mesh
2	5	30	2.5	475	-
1.66	6	36	3	420	13.1
1.25	8	48	4	409	2.7
1	10	60	5	399	2.5
0.66	15	90	5	361	10.5

Figure 27: Numerical residual velocity prediction with Lambert-Jonas V_{BL} fit with parameters given in the legend (a, p, V_{BL}).

10 mm thick laminates were also impacted with a 20 mm FSP at 300 m/s to investigate the unperforated response of thinner laminates. It was found that reducing the mesh size induced earlier failure of the target strike face (Table 9), which is consistent with previous DOP studies in the progressive failure regime (Table 7). This increased the BFD of the remaining laminate thickness deforming in a bulging manner, and may play a significant role in the variation of V_{BL} of thinner laminates as additional failed layers account for ≈ 10% of the laminate thickness, roughly equal to the reduction in ballistic limit (Table 8).

Table 9: Mesh sensitivity of BFD for a 10 mm laminate target impacted at 300 m/s.

Impact Zone Element Size (mm)	No. Sub-Laminates	K_I (N/mm³)	Outer Element Aspect Ratio	Maximum BFD (mm)	% Diff' from next largest mesh	DOP (mm)
2	5	30	2.5	42.87	-	0
1.66	6	36	3	42.31	0.1	0
1.25	8	48	4	46.13	8.3	2.5
1	10	60	5	50.12	8.0	3
0.66	15	90	5	52.91	5.3	4

Following the mesh studies, a 1 mm central mesh with a bias to 5 mm at the outer edge was selected for use in all further analyses. This appeared to show mesh convergence during DOP studies, whilst V_{BL} and BFD are within 10% of surrounding mesh sizes, whilst achieving reasonable computational run times. Typical runtimes for a 10 mm target with a 1 mm central mesh size were approximately 4 to 6 hours dependent on impact velocity.

5.3   Model-Experimental Comparison

Investigation at a range of non-dimensional areal densities was performed and compared with previous experimental results and analytical methods, with V_{BL} approximations from the model provided in Figure 28. Initial results gave good correlation between experimental results and the model, with increasing ballistic limit with increasing target thickness. The different mechanisms of energy absorption were also captured, bridging the gap between analytical models at non-dimensional areal densities ≈ 0.1. The model does however produce lower than expected V_{BL} at higher non-dimensional areal densities ($AD_t.A_p/m_p$) when compared with experimental results from literature, shown in Figure 29, where AD_t is the areal density of the target, A_p is the projected area of the projectile, and m_p is the mass of the projectile. Lassig *et al* [17] incorporated the Mie-Gruneisen equation of state into a ballistic impact model for Dyneema® and its effect on V_{BL} at higher impact speeds following its inclusion. At higher non-dimensional areal densities, the impact velocity required to perforate the target rises and shock effects become increasingly important.
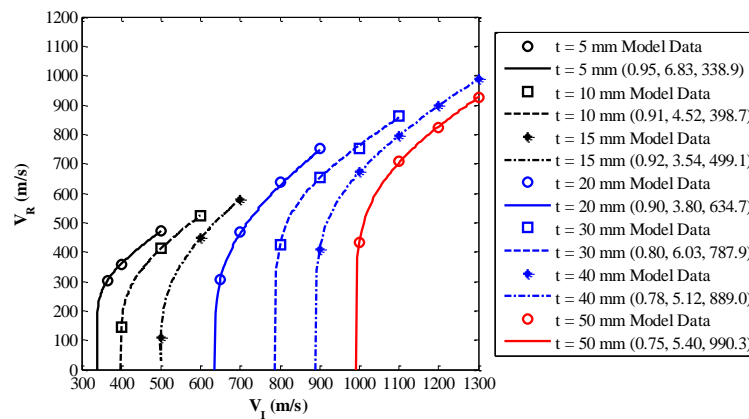

Figure 28: Lambert-Jonas ballistic approximation from model impacts with varying thickness t, with curve fit parameters given in the legend (a, p, V_BL).
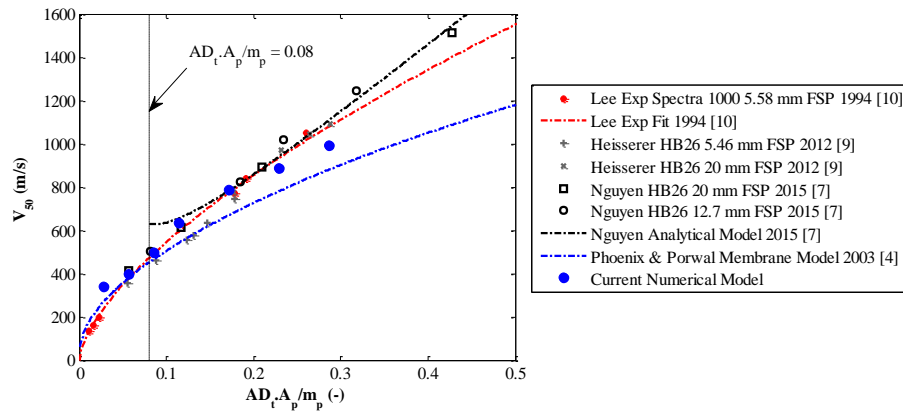
Figure 29: Experimental, analytical, and numerical ballistic limit compared in terms of non-dimensioned areal density.

5.4   Deformation and Failure Mechanisms of Laminates

BFD and shear hinge progression was compared with experimental results from Nguyen *et al* [3], showing good correlation to experimental results for a 10 mm target thickness for both BFD and shear hinge expansion (Figure 30b-c). At a greater target thickness of 20 mm and higher impact velocity, a larger BFD was predicted by the model (Figure 30d), supporting previous observations of over perforation at larger target thicknesses and higher impact velocities. A third result at 36 mm thickness and 888 m/s impact velocity showed complete perforation, whilst experimental results showed an unperforated response [3]. Thicker laminates ($\geq$ 20 mm) impacted at higher velocities ($\geq$ 600 m/s) have a larger portion of the laminate failing in a locally progressive manner around the projectile, with thinner laminates having a higher proportion of the laminate in bulging membrane action (Figure 31). This suggests a lower energy absorption during localised failure compared with experimental results. Large amounts of in-plane shear pull in was visible during bulging of the rear surface on all models during bulge deformation. This helped form the pyramid BFD shape observed in $[0°/90°]_n$ cross-ply ballistic impacts due to large anisotropy in the cross-ply [7]. In the transition zone from progressive local failure on the front face to bulging membrane action, large amounts of delamination was also visible, similar to that observed during experiments [14]. Minimal deformation of thicker laminates on the front surface was observed surrounding the impact zone, however thinner laminates tended to delaminate on the top surface following the direction of fibres that were in contact with the projectile. At the largest target thickness investigated (50 mm shown in Figure 31), increased projectile deformation was also visible, with blunting

of sharp edges of the 20 mm FSP observed at an impact speed of 900 m/s, similar to that observed during experiments [3].
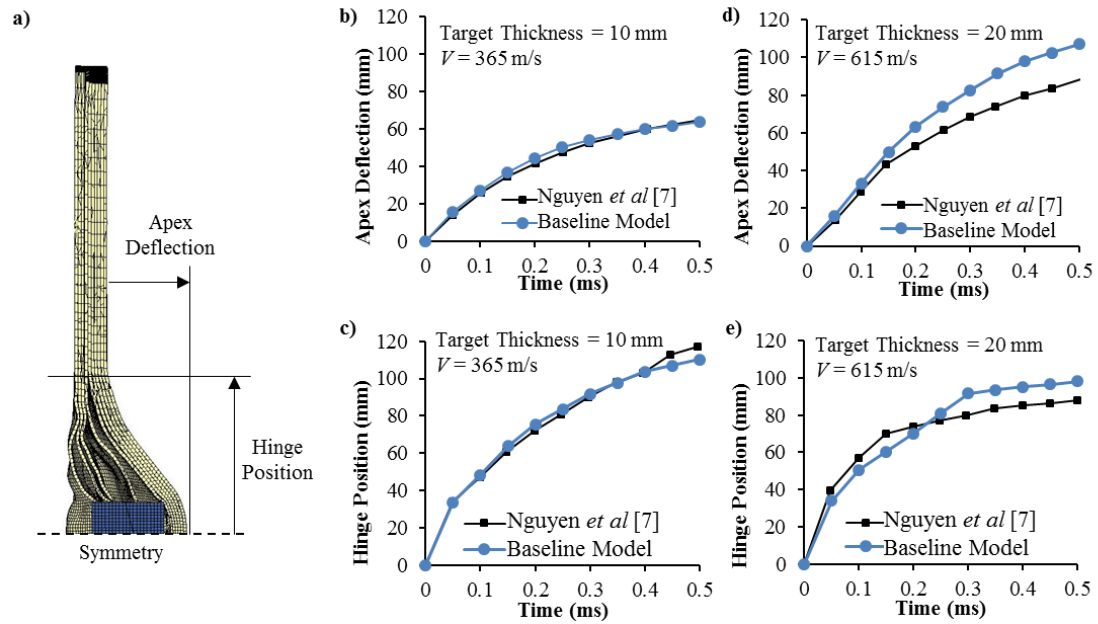

Figure 30: a) Schematic of apex deflection and hinge position, progression with time for b-c) 10 mm target at 365 m/s impact velocity and d-e) 20 mm target at 615 m/s impact velocity.
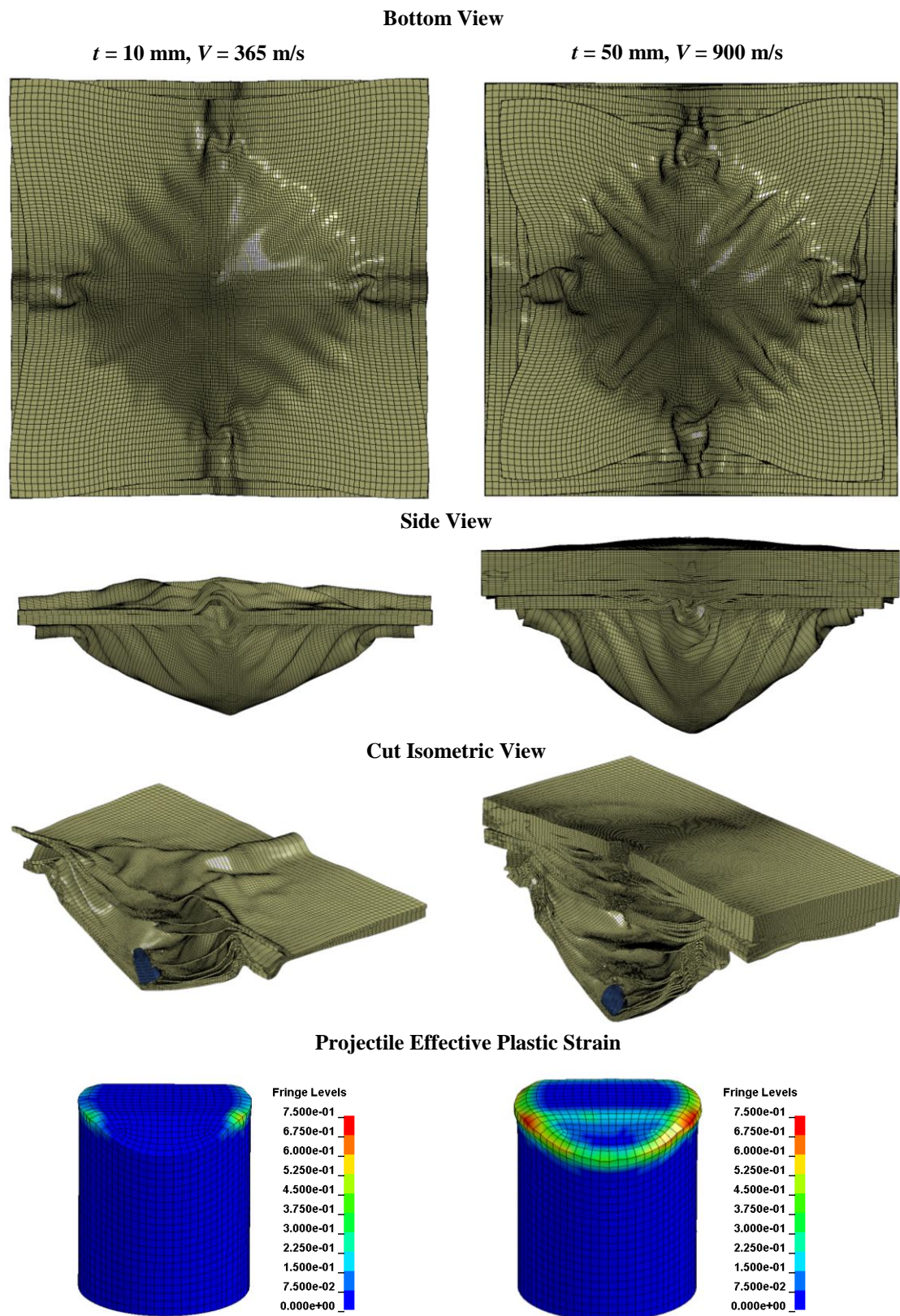
Bottom View

t = 10 mm, *V* = 365 m/s   *t* = 50 mm, *V* = 900 m/s

Side View

Cut Isometric View

Projectile Effective Plastic Strain

Figure 31: Model imagery of partially perforated 10 and 50 mm thick laminates at 0.5 ms after impact at 365 and 900 m/s respectively.

An investigation of the mechanism triggering change in failure mode from local progressive failure where effective fibre failure occurs to bulge and membrane action was performed using a 900 m/s FSP impact on a 50 mm thick laminate. It was observed that the reflective tensile relief wave [34] arrived at the progressively penetrating projectile front in under 40 µs, substantially reducing contact force on the projectile from the laminate (Figure 32). However, the projectile continues to fail plies in a progressive manner, indicating that the tensile relief wave is only one factor in controlling the transition from progressive local failure to bulge deformation. In the 50 mm target model, the projectile force at which the mode switch was observed is approximately 90 kN (≈ 286 MPa pressure assuming the FSP projected circumferential area) and at a later time than shown in Figure 32. Furthermore, some sub-laminates ahead of the one in direct contact with the projectile were also observed to be damaged by the high-pressure front prior to tensile relief wave interaction (Figure 32). This indicates that some damage may be imparted to the laminate by the compressive shockwave, prior to projectile interaction in that part of the laminate.
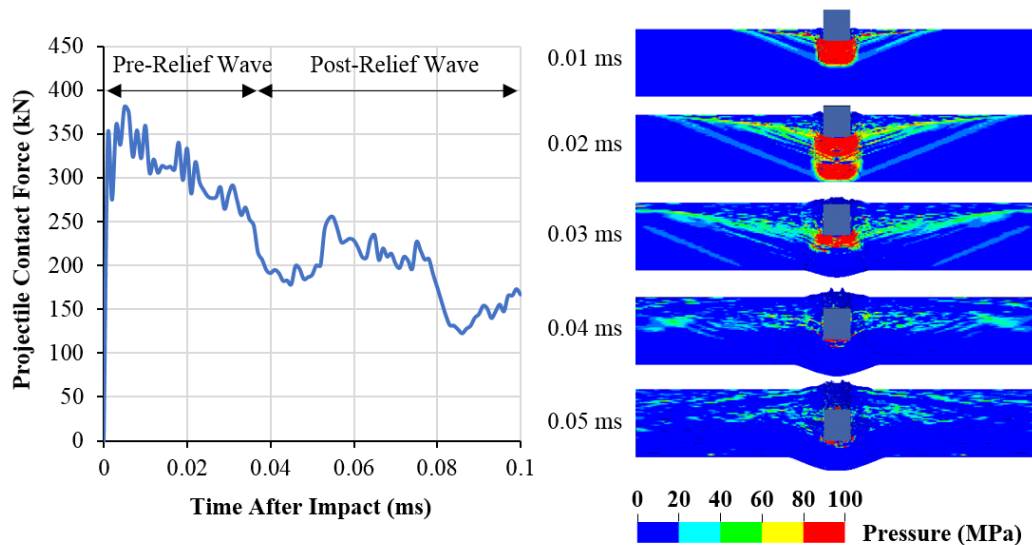

Figure 32: Projectile contact force against a 50 mm target laminate at 900 m/s impact speed with time, highlighting the arrival time of the reflected pressure relief wave.

6   Conclusions

A finite element modelling approach within LS-DYNA has been proposed to capture quasi-static stiffness behaviour, drop-weight impact behaviour, and finally ballistic behaviour of Dyneema® composites. Beam

studies highlighted the importance of the cohesive interface properties in limiting load transfer between sub-laminates and determining the stiffness response. Longer beam performance was determined by buckling at the root, with initiation load found to be dependent on fibre waviness. Drop weight impact modelling provided BFD and impactor contact force within 10% of that observed experimentally, with discrepancies thought to be caused by the difficulty in accurately capturing boundary conditions and the inability to capture microscale wrinkling phenomena in a larger continuum model. The magnitude and distribution of in-plane shear strain contour maps was similar between experimental digital image correlation and model output. Small differences arise as the complex in-plane shear response is not fully captured by the material model, and may be an area for future improvement. Ballistic performance in terms of V_{BL} and BFD was shown to be accurate at areal densities less than 0.15 $AD_t A_P/m_p$ and impact speeds less than 600 m/s. At lower target thickness and lower impact speeds, membrane and bulge deformation dominated the response. At higher areal densities, the ballistic limit from the model was lower than experimental results, thought to be due to the increasing importance of an equation of state, currently absent within this model. The mechanisms of failure were similar to that observed in ballistic impact, with large scale delamination, shear pull-in, and fibre failure all visible within the model. Mode switch between local progressive failure and bulge deformation was thought to be caused by reaching a critical contact force between the projectile and the laminate, below which the laminate can behave in a bulge deformation.

7   Acknowledgements

8   References

[1]   P.M. Cunniff. Dimensionless parameters for optimization of textile-based body armor systems, in *Proceedings of the 18th International Symposium on Ballistics*, 1999, pp. 1303–10.

[2]   T. Lässig, L. Nguyen, M. May, W. Riedel, U. Heisserer, H. van der Werff, S. Hiermaier. A non-linear orthotropic hydrocode model for ultra-high molecular weight polyethylene in impact simulations, *International Journal of Impact Engineering*, vol. 75, pp. 110–122, 2015.

[3]   L. Nguyen, T. Lässig, S. Ryan, W. Riedel. A methodology for hydrocode analysis of ultra-high molecular weight polyethylene composite under ballistic impact, *Composites Part A: Applied Science and Manufacturing*, vol. 84, pp. 224–235, 2016.

[4]   S.L. Phoenix, P. Porwal. A new membrane model for the ballistic impact response and V50 performance of multi-ply fibrous systems, *International Journal of Solids and Structures*, no. 40 (24), pp. 6723–6765, 2003.

[5]   G. Liu, M. Thouless. Collapse of a composite beam made from ultra high molecular-weight polyethylene fibres, *Journal of the Mechanics and Physics of Solids*, vol. 63, pp. 320–335, 2014.

[6]   M.K. Hazzard, S. Hallett, P.T. Curtis, L. Iannucci, R.S. Trask. Effect of Fibre Orientation on the Low Velocity Impact Response of Thin Dyneema® Composite Laminates, *International Journal of Impact Engineering*, vol. 100, pp. 35–45, 2016, (doi: 10.1016/j.ijimpeng.2016.10.007).

[7]   L. Nguyen, S. Ryan, S. Cimpoeru. The effect of target thickness on the ballistic performance of ultra high molecular weight polyethylene composite, *International Journal of Impact Engineering*, vol. 75, pp. 174–183, 2015.

[8]   T. Ćwik, L. Iannucci, P. Curtis, D. Pope. Investigation of the ballistic performance of ultra high molecular weight polyethylene composite panels, *Composite Structures*, vol. 149, pp. 197–212, 2016.

[9]   U. Heisserer, H. van der Werff. The relation between Dyneema® fiber properties and ballistic protection performance of its fiber composites, in *15th International Conference on Deformation, Yield and Fracture of Polymers*, 2012, vol. 3, pp. 242–246.

[10]   B.L. Lee, J.W. Song, J.E. Ward. Failure of spectra® polyethylene fiber-reinforced composites under ballistic impact loading, *Journal of Composite Materials*, vol. 28, no. 13, pp. 1202–1226, 1994.

[11]   G. Liu. Modelling microbuckling failure of a composite cantilever beam made from ultra high molecular-weight polyethylene fibres, *Acta Mechanica*, vol. 226, no. 4, pp. 1255–1266, 2015.

[12]   O. Nazarian, F. Zok. Constitutive model for the shear response of Dyneema® fiber composites, *Composites Part A: Applied Science and Manufacturing*, vol. 66, pp. 73–81, 2014.

[13]   S. Chocron, A.E. Nicholls, A. Brill, A. Malka, T. Namir, D. Havazelet, H. van der Werff, U. Heisserer, J.D. Walker. Modeling unidirectional composites by bundling fibers into strips with experimental determination of shear and compression properties at high pressures, *Composites Science and Technology*, vol. 101, pp. 32–40, 2014, (doi: 10.1016/j.compscitech.2014.06.016).

[14]   K. Karthikeyan, B.P. Russell, N.A. Fleck, H.N.G. Wadley, V.S. Deshpande. The effect of shear strength on the ballistic response of laminated composite plates, *European Journal of Mechanics - A/Solids*, vol. 42, pp. 35–53, 2013, (doi: 10.1016/j.euromechsol.2013.04.002).

[15]   M. Grujicic, P.S. Glomski, T. He, G. Arakere, W.C. Bell, B.A. Cheeseman. Material modeling and ballistic-resistance analysis of armor-grade composites reinforced with high-performance fibers, *Journal of Materials Engineering and Performance*, vol. 18, no. 9, pp. 1169–1182, 2009.

[16]   L. Iannucci, D. Pope, M. Dalzell, P. Dstl, W. Salisbury. A Constitutive Model for Dyneema UD composites, in *iccm-central.org*, 2009.

[17]   L. Nguyen, T. Lässig, S. Ryan. Numerical Modelling of Ultra-High Molecular Weight Polyethylene Composite under Impact Loading, in *the 13th Hypervelocity Impact Symposium*, 2015, pp. 436–443.

[18]   Materials Sciences Corporation, 135 Rock Rd, Horsham, Pennsylvania 19044. .

[19]   Z. Hashin. Failure criteria for unidirectional fiber composites, *Journal of applied mechanics*, vol. 47, no. 2, pp. 329–334, 1980.

[20]   B.A. Gama. *User Manual: A Progressive Composite Damage Model For Unidirectional and woven fabric*, no. 215. Materials Sciences Corporation (MSC) & University of Delaware Center for Composite Materials (UD-CCM), 2015.

[21]   J. Xiao, B. Gama, J. Gillespie. Progressive damage and delamination in plain weave S-2 glass/SC-15 composites under quasi-static punch-shear loading, *Composite Structures*, 2007.

[22]   T. Belytschko, L. Bindeman. Assumed strain stabilization of the eight node hexahedral element, *Computer Methods in Applied Mechanics and Engineering*, vol. 105, pp. 225–260, 1993.

[23]   B.P. Russell, K. Karthikeyan, V.S. Deshpande, N.A. Fleck. The high strain rate response of Ultra High Molecular-weight Polyethylene: From fibre to laminate, *International Journal of Impact Engineering*, vol. 60, pp. 1–9, 2013, (doi: 10.1016/j.ijimpeng.2013.03.010).

[24]   M.K. Hazzard, P.T. Curtis, L. Iannucci, S. Hallett, R. Trask. An Investigation of the in-plane performance of ultra-high molecular weight polyethylene fibre composites, in *International Conference of Composite Materials*, Copenhagen, 2015, pp. 19–24.

[25]   U. Heisserer, H. van der Werff. Strength Matters: Which Strength of Dyneema Fiber Composites to Use in Hydrocode Models? A Discussion., in *Internation Ballistics Symposium*, Edinburgh, 2016, no. Iso 527, pp. 1–5.

[26]   J.P. Attwood, S.N. Khaderi, K. Karthikeyan, N.A. Fleck, M.R. Omasta, H.N.G. Wadley, V.S. Deshpande. The out-of-plane compressive response of Dyneema ® composites, *Journal of the Mechanics and Physics of Solids*, vol. 70, pp. 200–226, 2014, (doi: 10.1016/j.jmps.2014.05.017).

[27]   B. Gama, J.W. Gillespie. Punch shear based penetration model of ballistic impact of thick-section composites, *Composite Structures*, 2008.

[28]   A. Levi-Sasson, I. Meshi, S. Mustacchi, I. Amarilio, D. Benes, V. Favorsky, R. Eliasy, J. Aboudi, R. Haj-Ali. Experimental determination of linear and nonlinear mechanical properties of laminated soft composite material system, *Composites Part B: Engineering*, vol. 57, pp. 96–104, 2014, (doi: 10.1016/j.compositesb.2013.09.043).

[29]   J. Attwood, N. Fleck. The compressive response of ultra-high molecular weight polyethylene fibres and composites, *International Journal of Solids and Structures*, vol. 71, pp. 141–155, 2015.

[30]   J. Hallquist. LS-DYNA keyword user's manual, *Livermore Software Technology Corporation*, 2007.

[31]   T. Lässig, F. Nolte, W. Riedel, M. May. An Assessment of Experimental Techniques For Measuring The Mode I Fracture Toughness Of UHMW-PE Composites, *Proceedings of the 17th European Conference on Composite Materials ECCM17*, 2016.

[32]   M. Grujicic, G. Arakere, T. He. Multi-scale ballistic material modeling of cross-plied compliant composites, *Composites Part B: Engineering*, vol. 40, no. 6, pp. 468–482, 2009.

[33]   J. Lambert, G. Jonas. Towards standardization in terminal ballistics testing: velocity representation, no. Technical report AD-A021 389. Ballistic Research Laboratories Aberdeen Proving Ground, MD, 1976.

[34]   L. Nguyen, S. Ryan, A.C. Orifici. A numerical investigation on the response of thick ultra-high molecular weight polyethylene composite to ballistic impact, *Proceedings - 29th International Symposium on Ballistics, BALLISTICS 2016*, vol. 2, 2016.